



AN EXPERIMENTAL STUDIE ON THE RHEOLOGY OF CUBIC BLUE PHASES

Aditya Saini

Research Scholar
Deptt. of Physics
Malvanchal University
Indore (M.P.)

Dr. V. K. Suman

Research Supervisor
Deptt. Of Physics
Malvanchal University
Indore (M.P.)

ABSTRACT:- The rheological characteristics of TGBA liquid crystals were the topic of our research in the chapter before this one. The rheology of yet another dissatisfied process of liquid crystals, namely that the blue phase, is the topic of discussion in this chapter. In this particular instance, the lattice of based on the following assumptions flaws serves to maintain the structure's integrity.

Blue phases, also known as BPs, are separate thermodynamic phases that can only be found in highly chiral liquid crystals and only exist within a very small temperature range (1 K). Friedrich Reinitzer was the first person to notice this phase in 1888. He was studying the melting behaviour of cholesteryl benzoate at the time, and he noticed that the material became blue and created a hazy condition as it was cooled [1]. For a very long time, researchers paid little attention to this particular condition of the liquid crystalline phase.

KEYWORDS:- Cubic Blue Phases, Thermodynamic

Introduction

The subsequent discovery of a polymer-stabilized blue phase that was stable across a broad temperature range sparked a tremendous amount of attention in the scientific community [2–10]. The blue phases are divided into three distinct categories according to their structures: BP-I, BP-II, and BP-III. Due to the amorphous nature of BP-III, its symmetry is identical to that of the isotropic phase. Due to the fact that it seems to be cloudy when seen via a polarising microscope, it might be difficult to recognise. The body-centered cubic structure is shown by BP-I, while the simple cubic structure is shown by BP-II.

In chapter 1, we went through the intricate structure of both of the blue phases, which we will refer to as BP-I and BP-II. Under a polarising microscope, both BP-I and BP-II are detectable and may be distinguished from one another. In general, BP-II may be detected throughout a specific range of chirality regimes, but it disappears in the high chirality regime. On the other hand, the stability of BP-I improves as the chirality of the system grows.

A massive amount of headway has been accomplished in the direction of comprehending the intricate structure of blue phases. There are still a great deal of basic facets of these strange phases that have not been studied. For instance, very lately, a number of estimates on the rheological characteristics and the dynamics of the disinclination networks of BP-I and BP-II were produced [11–13]. In spite of this, relatively little is known about just the rheological characteristics of these phases based on experimental research [14–16].

This chapter is dedicated to discussing the first in-depth experimental research ever conducted on the rheology of cubic blue phases. According to the findings of our research, the distinct rheological responses of BP-I and BP-II may be linked to the structures of these materials and the dynamics of defect networks.

Experimental

In this particular investigation, we employed a blue phase liquid crystal that consisted of a combination of four fluorinated chemicals and a highly chiral dopant. These chemicals were manufactured by our Polish colleagues who collaborated on this project. They do not degrade in the presence of chemicals and have a high resistance [17]. Below, in Fig. 4.1, you will see a precise molecular structure along with the weight percent of each individual component that makes up the combination.

The following phasing transitions are shown by it: I 46,4 degrees Celsius; BP-II 41,4 degrees Celsius; BP-I 36,6 degrees Celsius; N*. We carried out our rheological research by using a conflict rheometer that was equipped with a circular measuring device. The plate had a diameter of 25 millimetres, and the cone angle was 1 degree. The temperature of the material was maintained with an accuracy of 0.1 degrees Celsius throughout the experiment. In order to study the nanostructure as they were being sheared, we employed a system called rheo-microscopy.

Results and discussion

In the beginning, we used a polarised inverted microscope in a planar cell to examine the textures of the different phases that were present in our sample. BP-I and BP-II phases are shown in Fig. 4.12(a) and (b), respectively. One cholesteric (N) phase with an oily-streak imperfection network is shown in Fig. 4.12(c). The measurement plates of the rheometer were not given any kind of surface treatment before the aggregate sample was put on it.



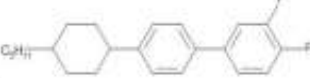

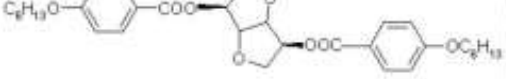
Chemical structure	Compounds	Concentration
	4'-(trans-4-Propylcyclohexyl)-3,4-difluorobiphenyl	19%
	4'-(trans-4-ethylcyclohexyl)-3,4-difluorobiphenyl	19%
	4'-(trans-4-pentylcyclohexyl)-3,4-difluorobiphenyl	38%
	4'-pentyl-4-fluorobiphenyl	4%
	3,6-bis-(4-hexyloxybenzoyl) isomannide	20%

Figure : The chemical structure and the wt% of individual compounds in the mixture, that shows blue phases.

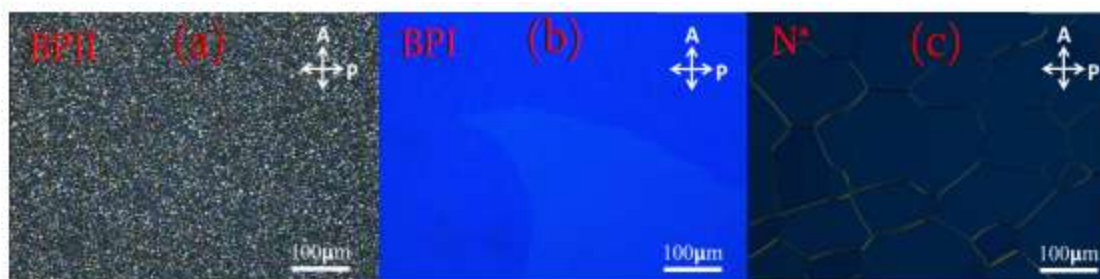


Figure : The textures of BP-II, BP-I and cholesteric (N *) phase observed under optical polarising microscope.

While the sample was in the isotropic state, we carried out all of the necessary measurements on it. In order to determine the temperatures at which the rheometer undergoes phase transitions, we first determined the temperature-dependent shear stress while maintaining a constant shear rate (Fig. 4.13). The transition from the isotropic (I) phase to the BP-II phase is characterised by a sudden rise in stress, while the transition from the BP-I phase to the cholesteric phase (N) is characterised by an abrupt decrease in the stress. During the transition from the BP-II to the BP-I phase, we noticed a little kink. The temperature range for BP-I is 4.8 degrees Celsius, whereas the temperature range for BP-II is 5 degrees Celsius. The stress in the N phase is virtually identical to the stress in the isotropic phase, with the exception of a progressive rise brought on by the reduction in temperature. It has come to our attention that the shear stress of the BP-I phase is much higher than that of the

BP-II phase and the N phase.

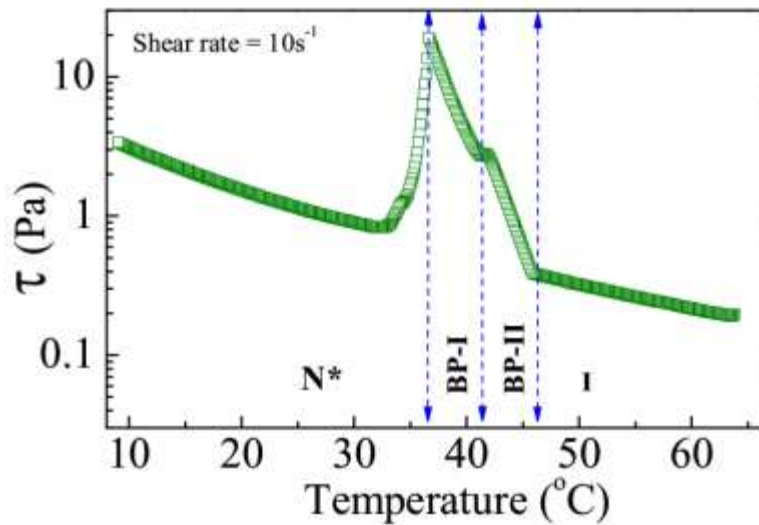


Figure: Temperature dependent shear stress at a constant shear rate (10 s^{-1}). Three different phase transitions are marked by dotted vertical lines.

Several example rheomicroscopy pictures were captured during the detection of temperature-dependent applied load at a given shear rate, and these images are shown in Figure 4.14. Within BP-II, we were able to identify the Grandjean-cano lines, which run in a direction that is orthogonal to the shear direction (Fig. 4.14(a)). It gives the impression that the director is oriented in a direction that is parallel to the shear direction. The mobility of these Grandjean-cano lines is the cause of the increase in shear stress that may be seen in comparison to the isotropic phase.

When compared to BP-II, BP-I begins to exhibit filamentary structures when the temperature is lowered (seen in Figure 4.14(b)), and it also begins to experience higher stress. During the time that the constant shear is taking place, these filamentary formations are continually broken and then reunited. The cholesteric phase demonstrates a typical texture (shown in Fig. 4.4(c) and (d)), which is analogous to the texture that is often seen under circumstances of planar degenerate surface anchoring.

Figure 4.15 illustrates the shear rate dependent viscosity of the material. We made the discovery that the N phase has a behaviour that is characteristic of shear thinning. In the low shear rate domain (ranging from 0.01 to 1 s^{-1}), the viscosities of the BP-II and BP-I phases are much higher than that of the N phase. For instance, when is equal to 0.01 s^{-1} , N is equal to 1.2 Pa s , BP II is equal to 17 Pa s , and BP I is equal to 52 Pa s . Both BP-I and BP-II exhibit numerous shear thinning behaviours, and the slope of varies depending on the value of. When subjected

to the greatest shear rate, the BP-II phase exhibits a lower viscosity than the N phase does. Therefore, BP-II exhibits a more pronounced shear thinning tendency compared to the other two phases.

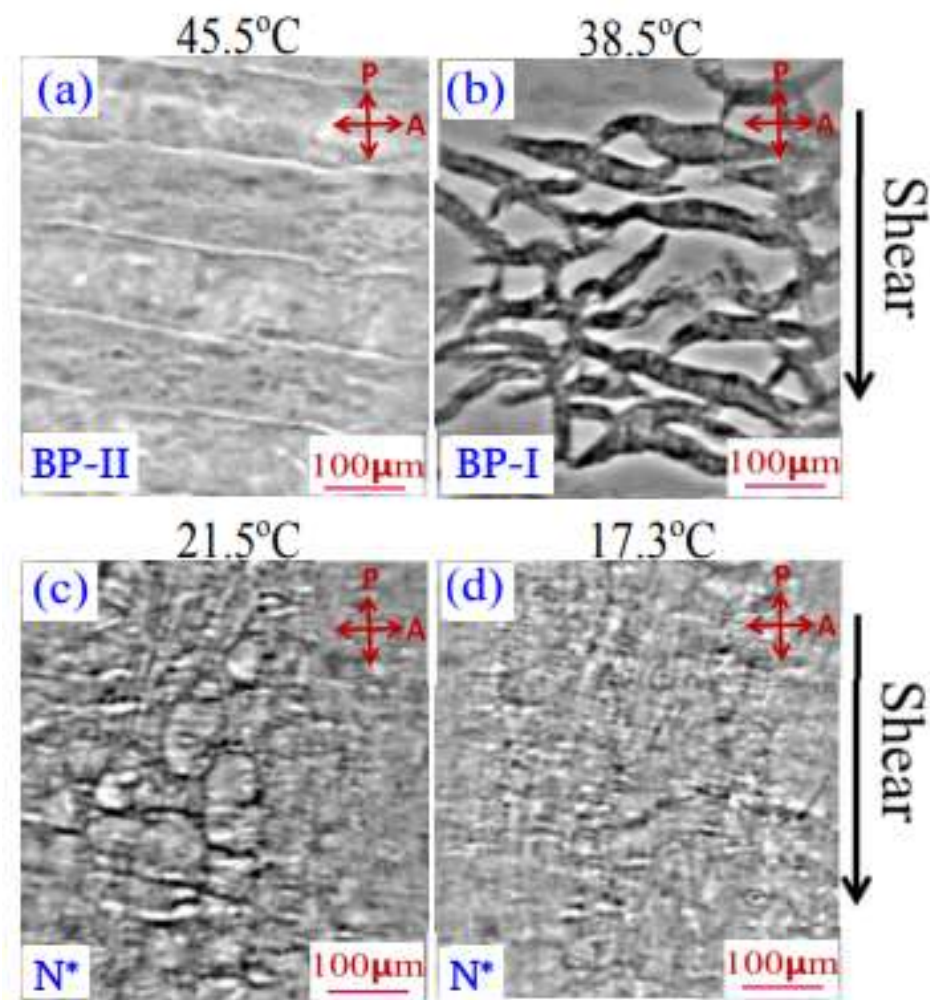


Figure: Optical rheomicroscopy images taken during the measurement of temperature dependent shear stress at a constant shear rate of 10 s^{-1} in three different phases. The direction of shear is shown by an arrow. P and A indicate polariser and analyser.

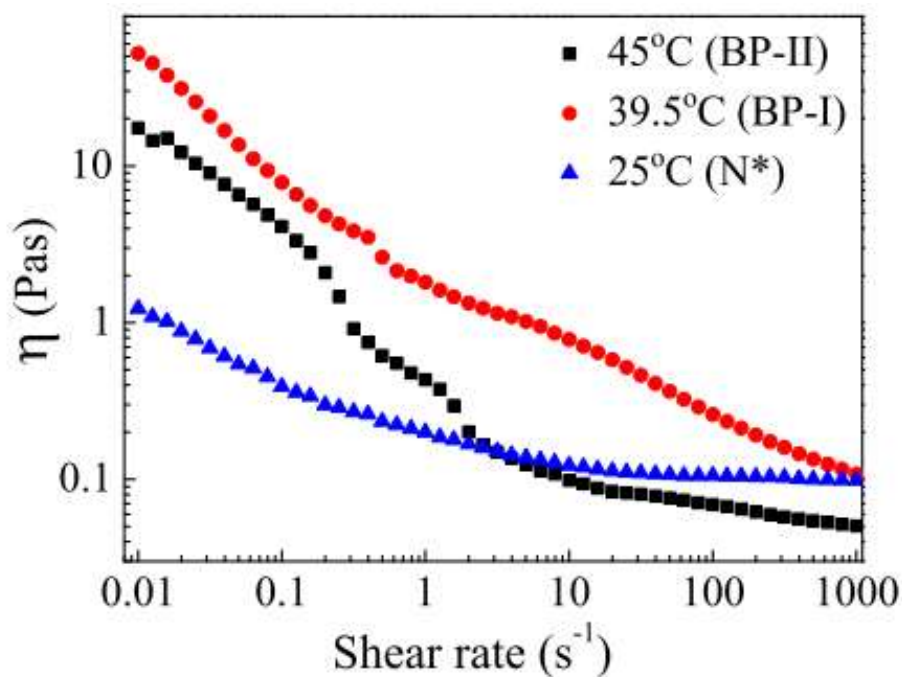


Figure 4.15: Shear rate dependent viscosity at three different temperatures representing BP-II, BP-I and N * phases.

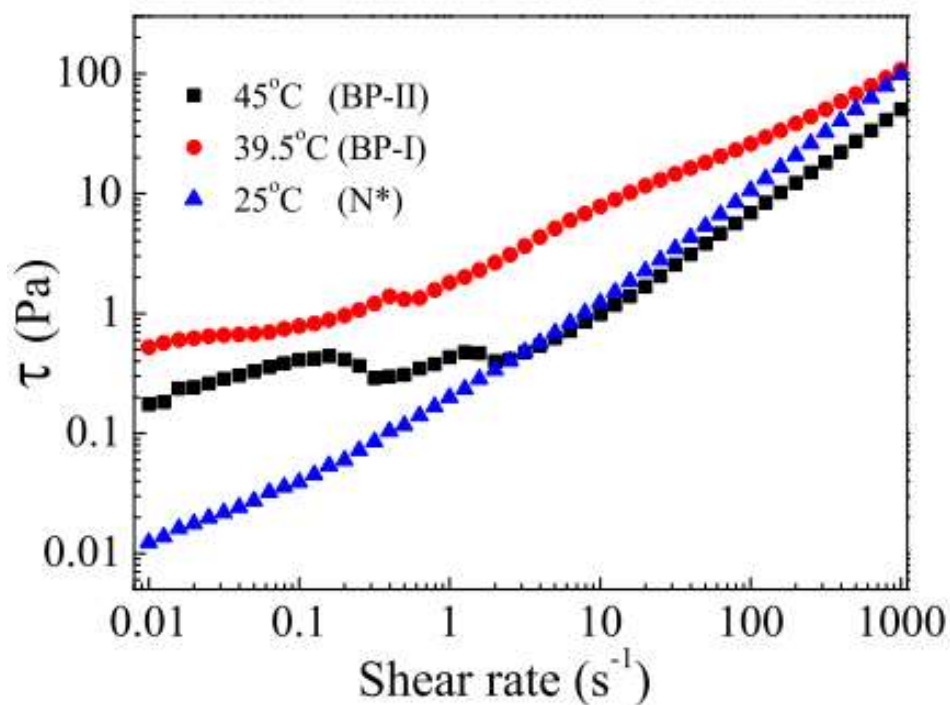


Figure 4.16: Shear rate dependent shear stress at three different temperatures representing BP-II, BP-I and N * phases.

In addition, we have calculated an approximation of the Ericksen number (Er) for each of the three phases, where even the elastic constant (K) of BP is of the order of 10^{11} N. The range of Ericksen numbers for the N phase ranges from 30 to 9 by 10^4 , and the shear rate may be anywhere from 0.01 to 1000 s^{-1} within this range. The ranges of the Ericksen number for the BP-II and BP-I are also the same: between 50 and $7 \cdot 10^4$ for the former, and between 300 and $1.2 \cdot 10^5$ for the latter. The big Ericksen overall number in the BP-I indicates that the shear viscosity is greater than the Totally honest elastic energy. This might be because of the filamentary crystal structures that were seen in Fig. 4.14. (b).

Figure 4.6 illustrates how the fracture stresses change in relation to the shear rate during the course of three phases. The shear stress of BP-II may be broken down into three separate regimes, which are denoted as follows: BP-II(1): = 0.01–0.3 s^{-1} ; BP-II(2): = 0.3–2 s^{-1} ; and BP-II(3): = 2–1000 s^{-1} . The data may be described with a very good approximation using a power law fit, which looks like this: $\tau = a \dot{\gamma}^b$ (Fig. 4.7). The parameters that best describe the fit are as follows: in BP-II(1), $a = 0.87$ and $b = 0.33$; in BP-II(2), $a = 0.42$ and $b = 0.35$; and in BP-II, $a = 0.12$ and $b = 0.87$. (3).

In addition, some typical rheomicroscopy pictures are included in Fig. 4.18, which shows shear rates in one of three distinct ranges. During BP-II (0.01–0.3 s^{-1}), we made the discovery that the Grandjean-cano lines move in a direction that is perpendicular to the shear direction (downward green arrows in BP-II, Fig. 4.18). The Grandjean-cano lines are disrupted in the BP-II (0.3 – 2 s^{-1}) phase, and the texture in the BP-II (2 – 1000 s^{-1}) phase resembles a flow aligned nematic phase. Even though there are several regimes seen in BP-I, they are not as easily distinguishable from one another as those shown in BP-II.

In spite of this, it is abundantly obvious that the multiple shear thinning occurs as a result of the breaking of texture at various shear rates (BP-I in Fig. 4.8). Up to a shear rate of $10 s^{-1}$, the cholesteric phase displays consistent shear thinning behaviour, and there is no discernible change in the textures. When the shear rate is increased above this point, the helix begins to unwind, which results in the formation of a flow-induced nematic phase and a subsequent reduction in viscosity. Shear rates of more than 126 and 200 s^{-1} are required for the flow-induced nematic condition to become apparent in BP-I and BP-II, respectively. Recent research conducted by Henrich and colleagues [12] used numerical modelling to investigate the rheology of cubic blue phases.

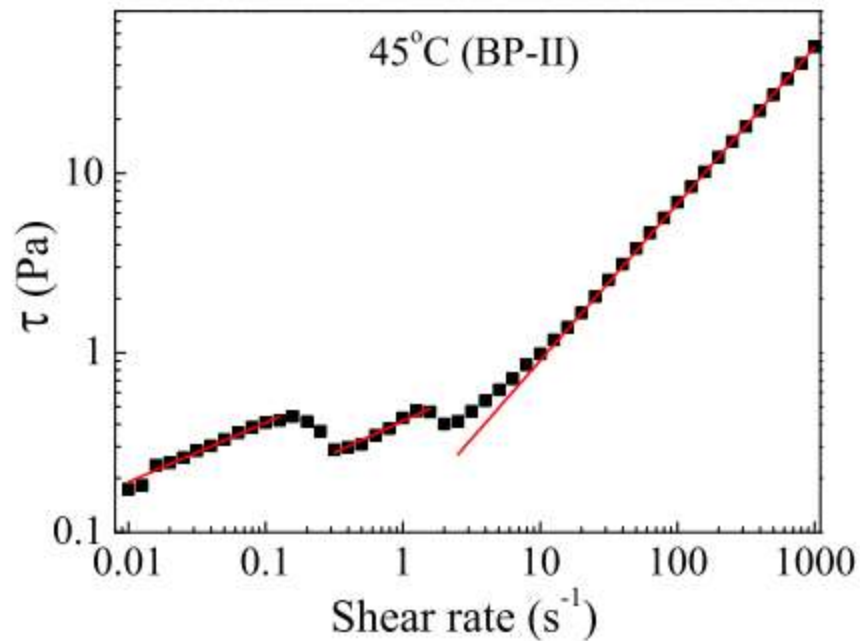


Figure: Shear rate dependent shear stress at 45°C (BP-II). Red lines are best fits to the power law: $\tau = a\dot{\gamma}^n$.

Both BP-I and BP-II have revealed a number of different flow regimes, and our findings qualitatively correspond with their assumptions, as shown in Fig. 4.19. These flow regimes are determined by the shear rate and the Ericksen number, respectively. In particular, we observed this phenomenon at substantially greater shear rates (ranging from 0.01 to 1000 s⁻¹) as opposed to what was predicted by the simulation. However, if the parameters are set up correctly, it should be able to witness the same phenomenon in the simulation at a considerably greater shear rate (just as in our experiment).

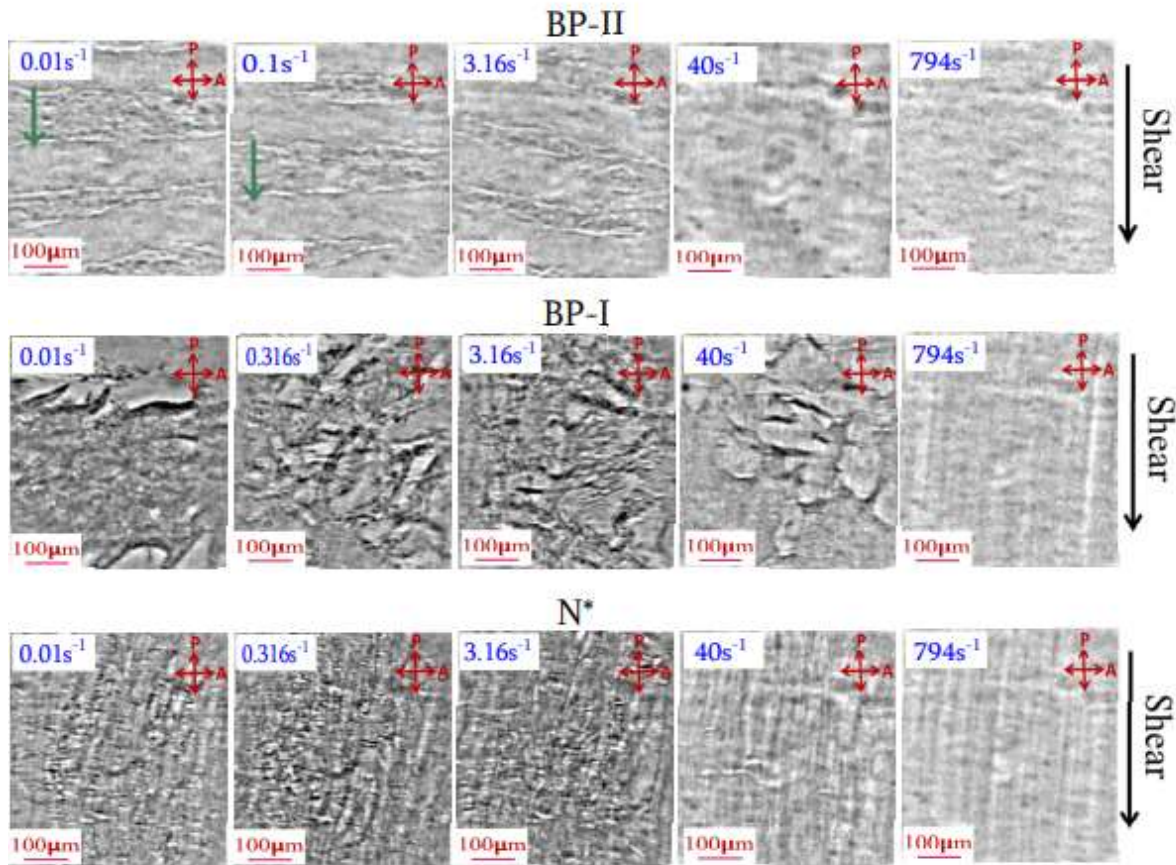


Figure : Rheomicroscopy images taken during the measurement of shear rate dependent viscosity in three phases. The direction of shear is shown by an arrow on the right side. The downward green arrows in BP-II show the motion of the Grandjean-cano lines.

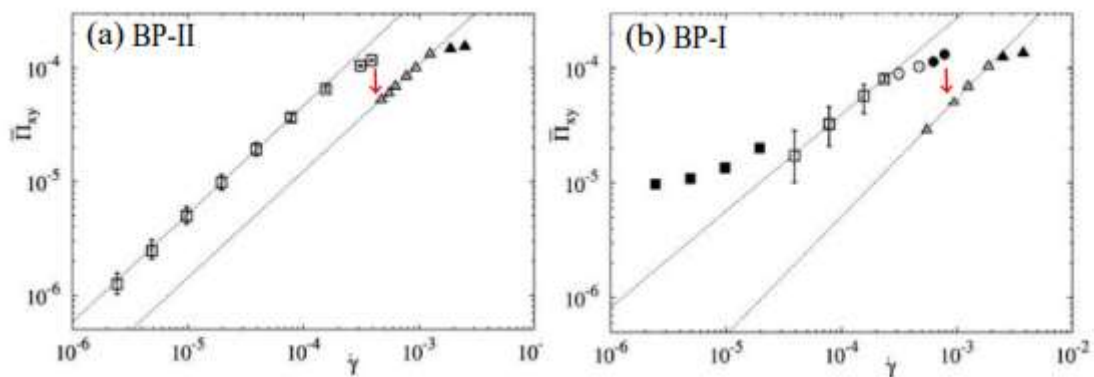


Figure : Flow curve of shear rate dependent shear stress showing various flow regimes of (a) BP-II and (b) BP-I. Above a critical shear rate the network breaks up into the Grandjean texture (open triangles) or a flow aligned nematic state at even higher shear rates (solid triangles). The red arrows indicate fall in

the shear stress values. Adapted from the ref. [12]

Experiments using small angle light scattering (SALS) were also carried out by our team. The information on the experimental set-up may be found in chapter 2 of the book. Figure 4.20 displays the pictures produced by HV scattering at a range of different shear speeds. We found that the SALS patterning of all of the phasing at the lowest loading stress (0.01 s1) are very often circular, with the N* phase having the biggest diameter. In contrast to the other phases, it seems that the orientational changes are more pronounced in the N phase. It's interesting to see that BP-II displays indistinct butterfly images at higher shear speeds (between 40 and 126 s⁻¹). In the plot, the dragonfly patterns stand out quite clearly (insets of Fig. 4.10, BP-II). Because of the density or inhibition perturbations that are reasonably coupled here to flow, those certain kinds of SALS configurations are typically seen in complex fluids such as hydrogel, polymer compositions, micellar detergents, and lyotropic fibrils phases [18,19]. Other examples of complex fluids that can exhibit SALS patterns include solvent mixture and polymer mixes.

On the other hand, when we performed rheomicroscopy at the identical shear rates, we did not see any unusual features. It seems to imply that the typical time of flow is much quicker than the time it takes for the microstructures to break down and reconstruct. At a shear rate of 40 s⁻¹, BP-I displays various scattering patterns (BP.4.20, BP-I) that are strikingly dissimilar to those seen by BP-II. This is as a result of the more pronounced orientational fluctuations that were seen (Fig. 4.18, BP-I) in rheomicroscopy. These fluctuations were generated by bigger microstructures. An unidirectional scattering pattern is shown by N when the shear rate is 40 s⁻¹; this pattern is stretched in a direction that is transverse to the shear direction. When the shear rate is very high (for example, 631 s⁻¹), the scattering patterns of both the BP-II as well as N phases become extremely elongated when seen in the direction that is perpendicular to that same shear direction. Since the pictures are in q-space, the shear direction serves as the primary alignment for the director's overall positioning. At higher shear rates (for example, at 631 s⁻¹), the scattering intensity in BP-I is nearly negligible, and this might be attributed to the very low birefringence and the cessation of orientational variations due to the huge elastic modulus.

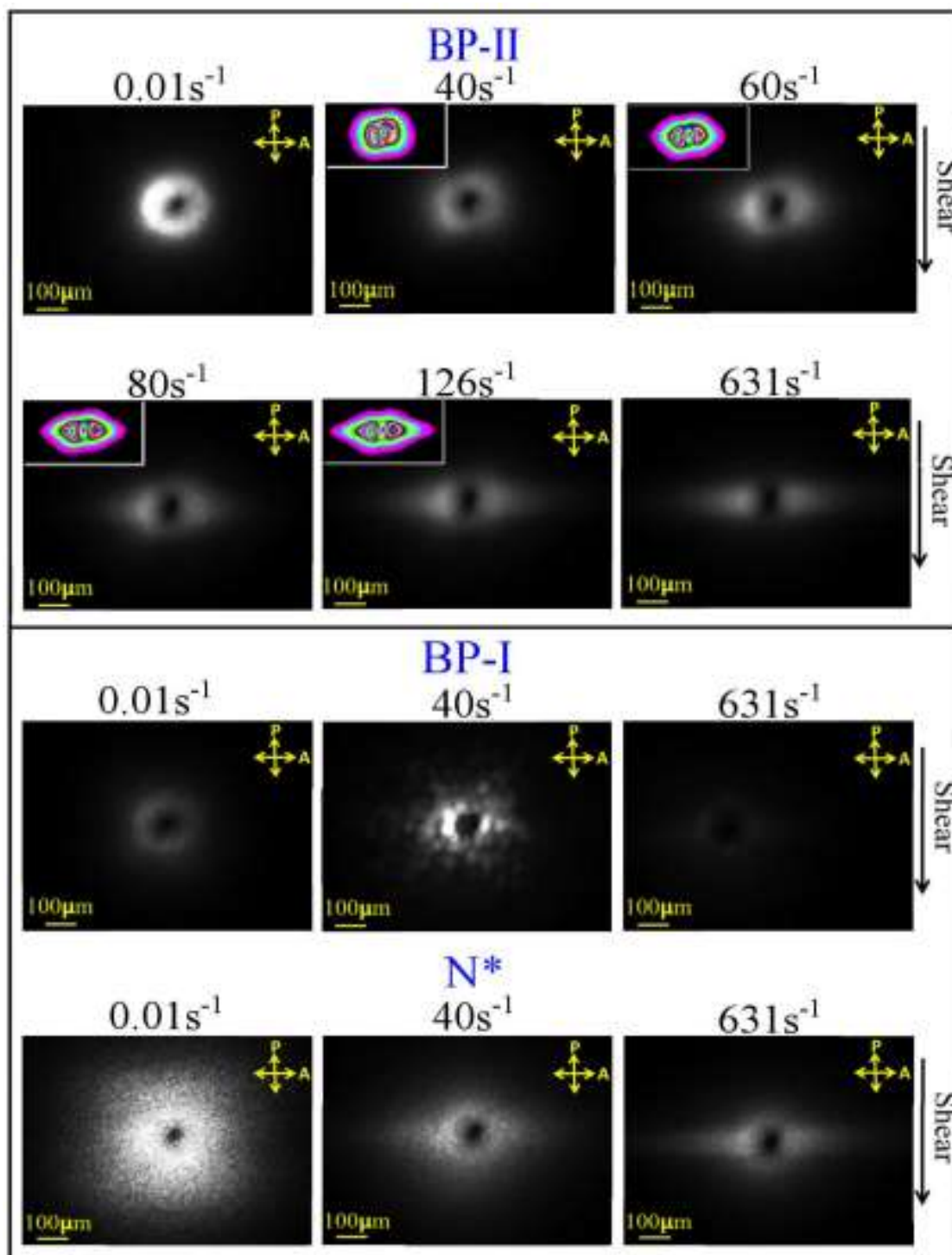


Figure : Small angle light scattering (SALS) images taken in the HV polarisation configuration at three different temperatures and various shear rates. The direction of shear is shown by an arrow. The insets are contour plots with false colours.

The strain variable storage moduli (G') or the loss moduli (G'') are shown in figure 4.21 for all of the episodes.

In the N phase, when the strain was low (1%), we found that the value of G' was less than G'' . In the maximum wear regime (more than 1%), G'' is bigger than G' ($G'' > G'$), and the material behaves in a manner that is characteristic of a fluid.

Each of the two blue phases, BP-I and BP-II, have a G' that is greater compared to the N phase, although the G' of BP-I is about five times bigger than that for BP-II. Both of these cubic phases have a nearly same linear piezoelectric (LVE) range (i.e., $c = 4\%$), which indicates that they are substantially identical. The strain-induced fluidisation, also known as the cross of G' and G'' , takes place at a strain value of = 16% in BP-I, but at a strain value of = 20% in BP-II. This is an increase from the strain value at which it takes place in BP-I.

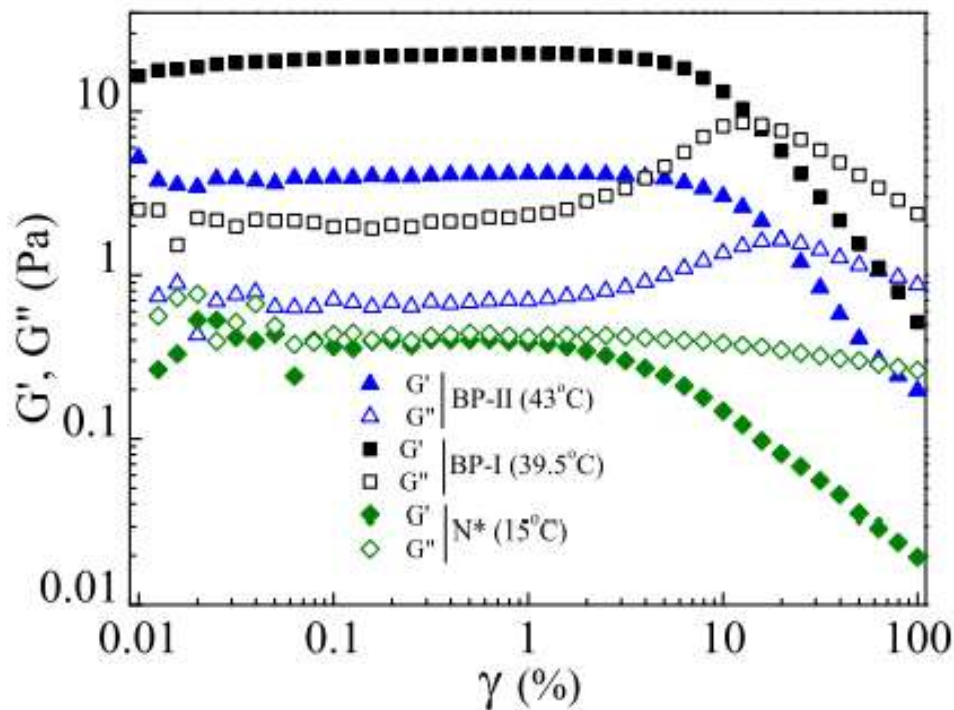


Figure : The strain dependence of the storage (G') and the loss (G'') moduli of the sample at three different temperatures where $\omega = 1 \text{ rad s}^{-1}$.

This might be because the defect lines in BP-II are crossing; as a result, a greater strain is required to break the overlap, and as a consequence, the critical strain amplitude of BP-II is greater than that of BP-I.

Step-strain measurements were carried out so that we could have a deeper understanding of the dynamic nature of the defect networks. Figure 4.22 illustrates the stress response that occurs when a step-strain is applied. In this instance, the value of strain was increased from 0.3% (within LVE) to 30%. (above LVE range). Within the time-dependent shear stress, there may be found three distinct zones. During the first 600 seconds of the first area

(region-I), the strain remains within the LVE range.

The strain is then kept constant for 600 seconds after being raised to a level that is higher than the LVE range (region-II), and then it is dropped to 0.3%. (region-III). The N phase exhibits the predicted stress response when a step strain is applied to any part of the material. It is possible that the breaking of defect nodes under high strain, which is then followed by continuous bulk flow, is the cause of a steady reduction in the amount of stress that can be seen in region-II of BP-II as time passes. Within the same area of BP-I, when the system is going through a flow aligned condition, the stress remains constant.

Because the faulty networks in question do not interact with one another, there is no possibility of their breaking. Both BP-I and BP-II exhibit sinusoidal stress oscillations in area III, which decrease in amplitude over the course of time. In BP-I, the amplitude of the oscillation is greater than what is seen in BP-II (Fig. 4.22, region-III). The periodic modulation in BP-I, which can be seen in area III of Fig. 4.22, is broken out into its own figure, which can be seen in Fig. 4.23.

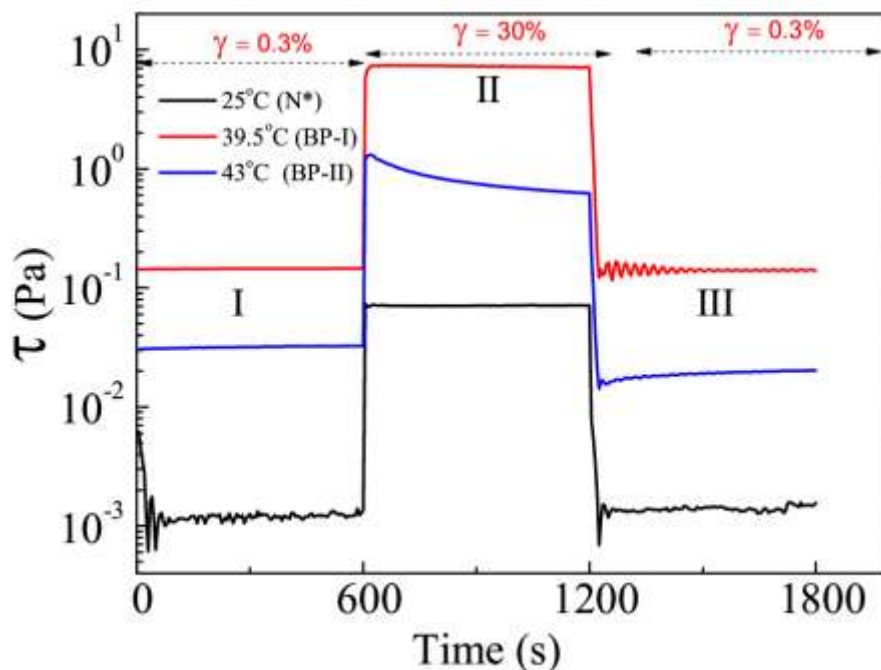


Figure : Time dependent shear stress at three different temperatures.

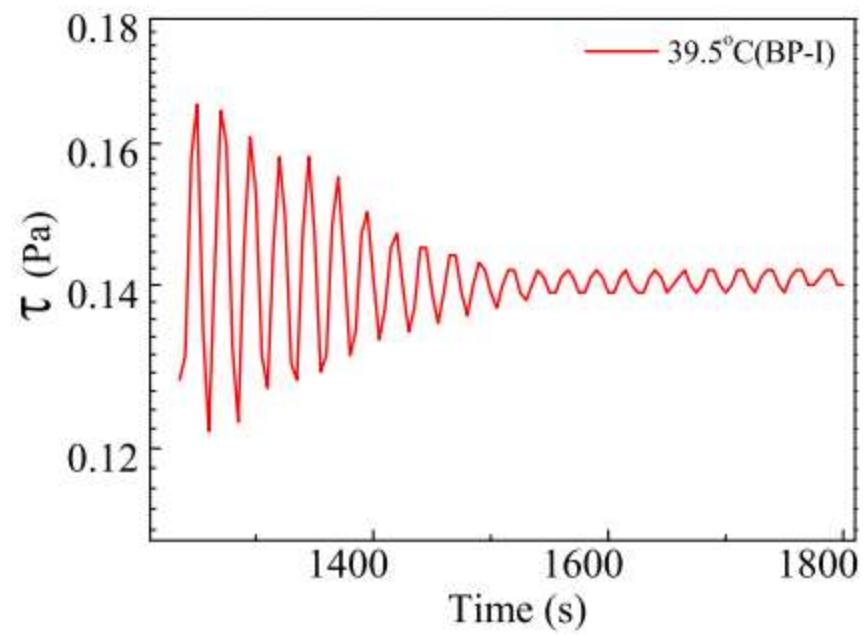


Figure : The periodic modulation in the BP-I, in region-III of Fig. 4.12.

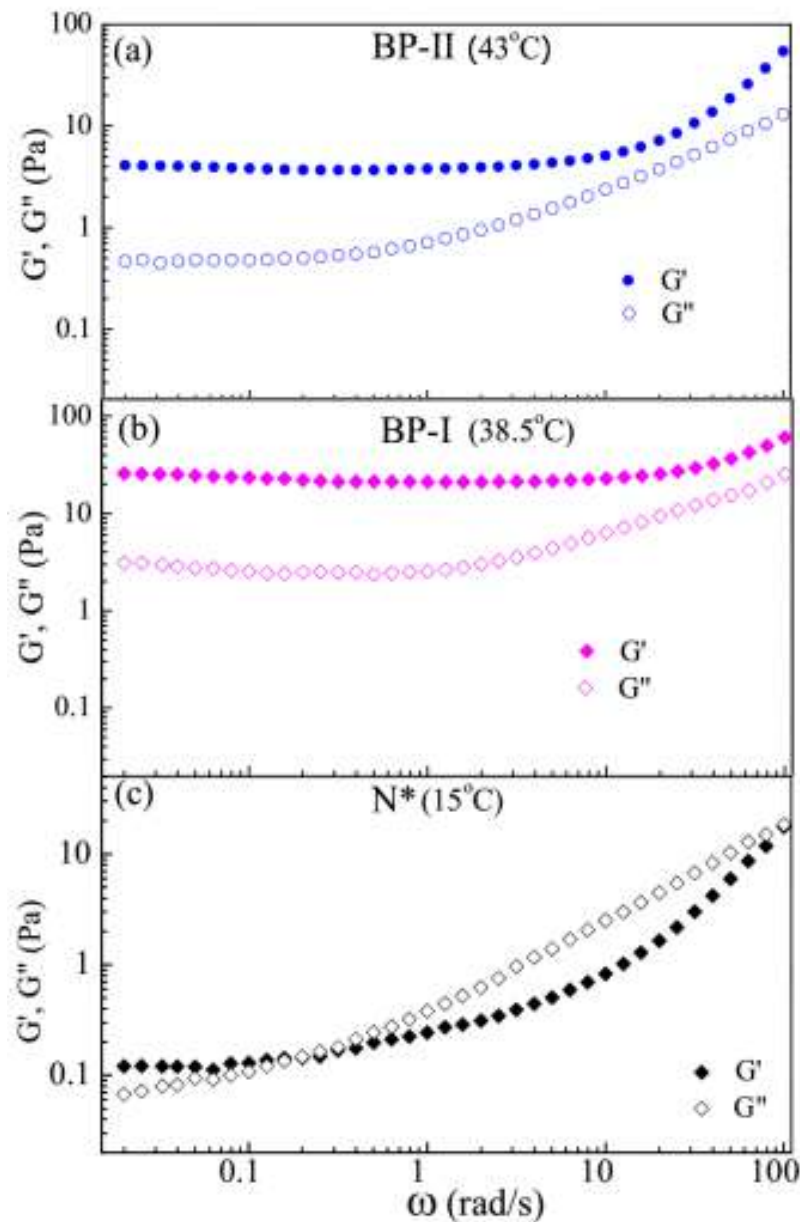


Figure: The frequency dependence of the storage (G') and the loss (G'') moduli of the sample at three different temperatures at a constant strain amplitude $\gamma = 1\%$.

In response to a significant strain, the deformities of BP-I move away from their equilibrium positions, which causes the network to become distorted. These defects have a tendency to reorganise themselves after the strain is removed, which may result in a periodic plastic strain oscillation that weakens over the course of time. It is possible that the reconnecting of certain faults is the cause of the minute oscillation that may be seen in area III of BP-II. We hypothesise that perhaps the step straining experiment demonstrates the distinct dynamical reactions of BP-I and BP-II under large strain, which are caused by the dissimilar network structures of the defects. These

responses are shown as a result of the step maximum stress experiment.

Last but not least, we have determined the frequency response of G' and G'' of all three phases (Fig. 4.24) by performing the measurements at a constant strain amplitude of 1%. [20] The cholesteric phase has a behaviour that is strikingly analogous to that of a gel. G' achieves a plateau at low frequency ($\omega = 0.2$), at which point $G' = G'' = 0.1$ Pa and the elastic modulus is greater than the loss modulus. At higher frequencies ($\omega > 0.2$), a fluid-like behaviour may be seen with G'' being bigger than G' . This occurs when G' is less than G'' . There is a transition that takes place at a critical frequency of $\omega = 0.2$ rad s⁻¹ between a solid-like regime in which $G' > G''$ and a fluid-like regime in which $G'' > G'$. This takes place from a solid-like regime to a fluid-like regime. In the case of BP-I and BP-II, G' is always higher than G'' , and the presence of a plateau indicates that both phases behave in a manner similar to a solid.

CONCLUSION

The rheological characteristics of cubic blue phases were investigated via experimentation. The results of our experiment show that there are many flow regimes, each of which has distinctive microstructures inside the blue phase. A flow centered nematic condition may be seen in all of the phases when the shear rate is sufficiently high. In BP-I, the apparent viscosity that was measured was higher than it was in BP-II. During the step stress changes, BP-I demonstrated a fading stress oscillate with time. This was coupled to the varied dynamical responsiveness of the defect circuits when they were subjected to significant strain. During the experiment with step strain, the magnitude of the rhythmic oscillations produced by BP-I is greater than that produced by BP-II. These findings are consistent with the most current simulation in a number of important respects. The fracturing of defect node is the cause of the greater critical strain seen in BP-II during the yield switch. The seeded region growing phase displays a behaviour similar to that of a gel, while BP-I and BP-II behave in a manner similar to that of an solid. Additionally, the deformation of BP-I is greater than that of BP-II.

REFERENCES:-

1. Acharya, A., & Dayal, K. (2013). Continuum mechanics of line defects in liquid crystals and liquid crystal elastomers. *Quarterly of Applied Mathematics*, 72(1), 33–64. <https://doi.org/10.1090/s0033-569x-2013-01322-x>
2. Basappa, G., Suneel, Kumaran, V., Nott, P. R., Ramaswamy, S., Naik, V. M., & Rout, D. (1999). Structure and rheology of the defect-gel states of pure and particle-dispersed lyotropic lamellar phases.

- European Physical Journal B*, 12(2), 269–276. <https://doi.org/10.1007/s100510051004>
3. Cao, M., Liu, S., Zhu, Q., Wang, Y., Ma, J., Li, Z., Chang, D., Zhu, E., Ming, X., Liu, Y., Jiang, Y., Xu, Z., & Gao, C. (2022). Monodomain Liquid Crystals of Two-Dimensional Sheets by Boundary-Free Sheargraphy. *Nano-Micro Letters*, 14(1), 1–13. <https://doi.org/10.1007/s40820-022-00925-2>
 4. Čopar, S., Kos, Ž., Emeršič, T., & Tkalec, U. (2020). Microfluidic control over topological states in channel-confined nematic flows. *Nature Communications*, 11(1), 1–10. <https://doi.org/10.1038/s41467-019-13789-9>
 5. Krakhalev, M. N., Bikbaev, R. G., Sutormin, Timofeev, I. V., & Zyryanov, V. Y. (2019). Nematic and cholesteric liquid crystal structures in cells with tangential-conical boundary conditions. *Crystals*, 9(5), 28–39. <https://doi.org/10.3390/cryst9050249>
 6. Kumar, N., Zhang, R., De Pablo, J. J., & Gardel, M. L. (2018). Tunable structure and dynamics of active liquid crystals. *Science Advances*, 4(10), 1–13. <https://doi.org/10.1126/sciadv.aat7779>
 7. Li, C. Y., Wang, X., Liang, X., Sun, J., Li, C. X., Zhang, S. F., Zhang, L. Y., Zhang, H. Q., & Yang, H. (2019). Electro-optical properties of a polymer dispersed and stabilized cholesteric liquid crystals system constructed by a stepwise UV-initiated radical/cationic polymerization. *Crystals*, 9(6), 20–27. <https://doi.org/10.3390/cryst9060282>
 8. Liu, Y., Li, Y., Chen, Q., Li, S., & Su, Y. (2019). Liquid crystal based head-up display with electrically controlled contrast ratio. *Crystals*, 9(6), 11–19. <https://doi.org/10.3390/cryst9060311>
 9. Loudet, J. C. (2005). Colloidal inclusions in liquid crystals: Phase separation mechanisms and some dynamical aspects. *Liquid Crystals Today*, 14(1), 1–14. <https://doi.org/10.1080/14625180500137803>
 10. Mitov, M. (2020). Advances in Cholesteric Liquid Crystals. In *Advances in Cholesteric Liquid Crystals*. <https://doi.org/10.3390/books978-3-03928-229-6>
 11. Ramos, L., Zapotocky, M., Lubensky, T. C., & Weitz, D. A. (2002a). Rheology of defect networks in cholesteric liquid crystals. *Physical Review E - Statistical Physics, Plasmas, Fluids, and Related Interdisciplinary Topics*, 66(3), 1–38. <https://doi.org/10.1103/PhysRevE.66.031711>
 12. Ramos, L., Zapotocky, M., Lubensky, T. C., & Weitz, D. A. (2002b). Rheology of defect networks in cholesteric liquid crystals. *Physical Review E - Statistical Physics, Plasmas, Fluids, and Related*

Interdisciplinary Topics, 66(3). <https://doi.org/10.1103/PhysRevE.66.031711>

13. Varney, M. C. M., Jenness, N. J., & Smalyukh, I. I. (2014). Geometrically unrestricted, topologically constrained control of liquid crystal defects using simultaneous holonomic magnetic and holographic optical manipulation. *Physical Review E - Statistical, Nonlinear, and Soft Matter Physics*, 89(2), 1–12. <https://doi.org/10.1103/PhysRevE.89.022505>
14. Wang, W., Zhang, L., & Zhang, P. (2021). Modelling and computation of liquid crystals. *Acta Numerica*, 30, 765–851. <https://doi.org/10.1017/S0962492921000088>
15. Wang, Z., Rofouie, P., & Rey, A. D. (2019). Surface anchoring effects on the formation of two-wavelength surface patterns in chiral liquid crystals. *Crystals*, 9(4), 40–61. <https://doi.org/10.3390/cryst9040190>
16. Wensink, H. H. (2019). Effect of size polydispersity on the pitch of nanorod cholesterics. *Crystals*, 9(3), 72–82. <https://doi.org/10.3390/cryst9030143>
17. Yevdokimov, Y., Skuridin, S., Salyanov, V., Semenov, S., & Kats, E. (2019). Liquid-crystalline dispersions of double-stranded DNA. *Crystals*, 9(3), 15–18. <https://doi.org/10.3390/cryst9030162>